

REST-FRAME OPTICAL EMISSION LINES IN $Z \sim 3.5$ LYMAN BREAK SELECTED GALAXIES: THE UBIQUITY OF UNUSUALLY HIGH [O III]/H β RATIOS AT 2 GYR^{1,2}

B. P. HOLDEN³, P. A. OESCH^{3,4}, V. G. GONZÁLEZ⁵, G. D. ILLINGWORTH³, I. LABBÉ⁶, R. BOUWENS⁶, M. FRANX⁶, P. VAN DOKKUM⁴, AND L. SPITLER^{7,8}

Draft version October 14, 2018

ABSTRACT

We present K -band spectra of rest-frame optical emission lines for 24 star-forming galaxies at $z \sim 3.2$ – 3.7 using MOSFIRE on the Keck 1 telescope. Strong rest-frame optical [O III] and H β emission lines were detected in 18 LBGs. The median flux ratio of [O III] λ 5007 to H β is $5.1^{+0.5}_{-0.5}$. This is a factor of 5–10 \times higher than in local galaxies with similar stellar masses. None of our sources are detected in deep X-ray stacks, ruling out significant contamination by active galactic nuclei. Combining our sample with a variety of LBGs from the literature, including 49 galaxies selected in a very similar manner, we find a high median ratio of [O III]/H β = $4.8^{+0.8}_{-1.7}$. This high ratio seems to be an ubiquitous feature of $z \sim 3$ – 4 LBGs, very different from typical local star-forming galaxies at similar stellar masses. The only comparable systems at $z \sim 0$ are those with similarly high specific star-formation rates, though $\sim 5\times$ lower stellar masses. High specific star-formation rates may result in a higher ionization parameter, higher electron density, or harder ionizing radiation, which, combined different elemental abundances, result in a much higher [O III]/H β line ratio. This implies a strong relation between a global property of a galaxy, the specific star-formation rate, and the local conditions of ISM in star-forming regions.

Subject headings: galaxies: evolution — galaxies: high-redshift — galaxies: spectroscopy

1. INTRODUCTION

Tracing out the star-formation history of the universe is a key ingredient for our understanding of the mass assembly of galaxies. Great progress has been made in the last decade or so based on deep imaging surveys both from the ground and from space with the Hubble Space Telescope (*HST*). These have led to the very efficient identification of several thousand star-forming galaxies at $z \geq 4$ based on broad-band imaging, using the Lyman break selection technique (e.g., Steidel et al. 1996). Thanks to the combination of *HST* and *Spitzer*/IRAC imaging, the analysis of these galaxies was further extended from rest-frame UV only studies

to include the rest-frame optical, leading to reliable estimates of the stellar mass functions of very faint galaxies out to $z \sim 7$ – 8 (e.g., Stark et al. 2009; Labbé et al. 2010a; González et al. 2012; Lee et al. 2012).

Since some of the strongest emission lines such as H α or [O III] λ 5007 are shifted into the observed-frame near-infrared at $z \gtrsim 2$, progress on spectroscopic confirmation and observation of rest-frame optical lines was very slow and time consuming. However, with the advent of efficient multi-object near-infrared spectrographs on 8m-class telescopes, this situation is now changing. In this paper we present an analysis of [O III] and H β emission lines of a sample of $z \sim 3.5$ galaxies based on observations with the Keck MOSFIRE instrument (McLean et al. 2012).

The strength of such lines is very important as they can provide key insight into the conditions of star-formation in high-redshift sources, and when combined with additional line measurements such as [O II] can provide an estimate of the gas-phase metallicity of $z \sim 3$ – 4 galaxies (e.g. Maiolino et al. 2008; Mannucci et al. 2009; Troncoso et al. 2013).

There is now growing evidence for a high fraction of galaxies showing strong nebular line emission at $z \sim 4$ – 8 , with median rest-frame equivalent widths (EW_0) of $\gtrsim 300$ Å (e.g., Schaerer & de Barros 2009; de Barros et al. 2012; Stark et al. 2013). From a sample of 74 isolated galaxies with deep *Spitzer*/IRAC photometry and with spectroscopic redshifts in the range $3.8 < z < 5.0$, Shim et al. (2011) find that 65% show clear flux excess in IRAC [3.6], indicative of strong H α emission. From this excess in the broad-band photometry, they estimate rest-frame equivalent widths in the range 140–1700 Å. In a similar analysis, Stark et al. (2013) derive the $EW(H\alpha)$ distribution at this redshift, finding a mean value of 270

¹ The data presented herein were obtained at the W.M. Keck Observatory, which is operated as a scientific partnership among the California Institute of Technology, the University of California and the National Aeronautics and Space Administration. The Observatory was made possible by the generous financial support of the W.M. Keck Foundation.

² Partially based on data obtained with the *Hubble Space Telescope* operated by AURA, Inc. for NASA under contract NAS5-26555. Partially based on observations with the *Spitzer Space Telescope*, which is operated by the Jet Propulsion Laboratory, California Institute of Technology under NASA contract 1407.

³ UCO/Lick Observatories, University of California, Santa Cruz, 95065; holden@ucolick.org, gdi@ucolick.org

⁴ Yale Center for Astronomy and Astrophysics, Dept. of Astronomy, Yale University; pascal.oesch@yale.edu, pieter.vandokkum@yale.edu

⁵ Dept. of Astronomy, University of California, Riverside; valentino.gonzalez@ucr.edu

⁶ Leiden Observatory, Leiden University, P.O. Box 9513, 2300 RA Leiden, The Netherlands; ivo@strw.leidenuniv.nl, franx@strw.leidenuniv.nl

⁷ Dept. of Physics and Astronomy, Macquarie University; lee.spitler@mq.edu.au

⁸ Australian Astronomical Observatory, North Ryde, Australia

Å. González et al. (2012) find a similar flux excess in the median stacked SEDs of galaxies at $z \sim 5, 6,$ and 7 (see also Labbé et al. 2012; Smit et al. 2013). This excess suggests that [OIII] and $H\beta$ also have large rest-frame EWs and that strong emission lines may be ubiquitous over a range of masses ($M = 10^9$ – $10^{10} M_\odot$). Most recently, Schenker et al. (2013) used a sample of 20 Lyman Break galaxies (LBGs) to spectroscopically confirm that the majority of $z \sim 3.5$ galaxies have strong [O III] equivalent widths in agreement with the $H\alpha$ equivalent width distribution based on the broad-band IRAC photometry.

In the local universe, galaxies with extreme emission lines have been identified from SDSS based on extremely blue $r - i$ colors because the r -band is dominated by the [OIII] line (Kakazu et al. 2007; Cardamone et al. 2009, e.g.). Such low-metallicity starbursts only contribute a small fraction of the total star-formation at $z < 1$. At higher redshift, $z \sim 1.7$, similar observations based on extreme broad band colors have revealed a significant population of galaxies that are undergoing vigorous star-formation episodes. This is indicated by their large [OIII] + $H\beta$ EWs ~ 1000 Å, that imply that they can build their whole stellar mass in only 15 Myr (van der Wel et al. 2011; Maseda et al. 2013). Similarly strong line emitters have independently been found even up to $z \sim 2.3$ from WFC3/IR grism spectroscopy (Atek et al. 2011; Xia et al. 2012). At these higher redshifts, the number density of such sources is found to be quite significant ($\sim 4 \times 10^{-4} \text{ Mpc}^{-3}$).

These strong emission lines point to unusual properties in the high redshift star-forming population. As an example, one can consider the Lynx arc, which in many ways is a prototypical galaxy at high redshift with unusual properties. Fosbury et al. (2003) studied this object with deep, high quality spectra across the rest-frame UV and optical. The galaxy shows strong ionization, such that the [O II] line is not detected despite the detection of the [Ne III] at 3869 Å. To reproduce these line strengths and ratios, a cluster of $\sim 10^5$ stars with surface temperatures of 80,000 K is required. An absorbed AGN could explain this source, though that possibility makes specific predictions (Binette et al. 2003).

It appears, however, that such objects are common at $z \sim 2$ (Nakajima et al. 2013) requiring different interstellar medium properties than we see in the local universe (Kewley et al. 2013b), potentially with significantly higher ionized gas densities (e.g. Shirazi et al. 2013). Recent theoretical models can reproduce such line ratios, but they require very different ionization parameters, strong winds, radiation pressure or significant shocks even at the low metallicity values expected for galaxies at such an early epoch in the universe (Yeh et al. 2013; Verdolini et al. 2013; Kewley et al. 2013a; Rich et al. 2014).

In this paper, we probe the star-formation properties of a sample of $z \sim 3.5$ star-forming galaxies with the use of Keck MOSFIRE multi-object near-infrared spectroscopy to target the [O III] and $H\beta$ lines with a single mask observation in the GOODS-South field. The paper is organized as follows: in Section 2, we present our target selection, before describing our observations in Section 3, and outlining our analysis in Section 4. Finally, we end with the presentation and a discussion

of our results in Section 5. Throughout this paper, we adopt AB magnitudes and a standard cosmology with $\Omega_M = 0.3, \Omega_\Lambda = 0.7,$ and $H_0 = 70 \text{ km s}^{-1} \text{ Mpc}^{-1}$.

2. TARGET SELECTION AND PHOTOMETRIC DATA

Our primary goal is to investigate the rest-frame optical emission line properties of Lyman break selected, star-forming galaxies at $z \sim 3.5$. The GOODS-South field offers the best combination of multi-wavelength imaging data both from the ground and from space with HST and Spitzer, as well as a large sample of spectroscopically confirmed LBGs in the required redshift range based on the large campaign of rest-frame UV spectra (e.g. Vanzella et al. 2008; Balestra et al. 2010).

2.1. Pre-Existing Spectroscopic Sample

The primary emission lines of our study are $H\beta$ and the [O III] $\lambda\lambda 4959, 5007$ doublet. These lines are accessible in the K band over the redshift range $3.2 < z < 3.8$. To increase the efficiency of our observations, we prioritized galaxies with existing spectroscopic redshifts such that their $H\beta$ and [O III] lines would fall in between the many strong night sky lines. To do this, we used the spectroscopic catalogs of GOODS-South compiled by Vanzella et al. (2008) and Balestra et al. (2010) who observed large samples of LBGs in this redshift range.

We identified an overdensity of galaxies in the South-West part of GOODS-South with existing spectroscopic redshifts for which our target lines would lie in between sky lines, and we thus chose to center our mask design around that apparent overdensity. We designed the mask to maximize the number of galaxies with known redshifts and were able to fit 15 into our design.

The rest-frame UV spectra of these galaxies show Lyman α in emission in 8 of the 15 galaxies, with measured equivalent widths ranging from 4 to 72 Å (measured from the spectra of Balestra et al. 2010; Vanzella et al. 2008).

In addition to the spectroscopically confirmed sample, we included nine B_{435} dropout galaxies without pre-existing rest-frame UV redshift measurements as secondary targets.

Since our input spectroscopic redshift samples are based on rest-frame UV spectra, we are selecting galaxies bright in the rest-frame UV, typically brighter than $i_{775} < 25$ mag AB (Balestra et al. 2010). These magnitudes imply star-formation rates of $\gtrsim 10 M_\odot \text{ yr}^{-1}$ which should yield solid detections for $H\beta$ (signal to noise > 7) in a 3 to 4 hour exposure with the MOSFIRE spectrograph. The filler galaxies were in general much fainter than the spectroscopic input sample. The final mask design included 24 high-redshift targets, in addition to one star for measuring the Telluric absorption.

2.2. Imaging Data and Photometry

All our targets are covered by multi-wavelength imaging data from HST. We use our own reduction of the GOODS-South ACS data, which includes additional follow-up observations and is therefore somewhat deeper than the publicly available v2.0 images (Giavalisco et al. 2004), reaching to $i_{775} = 28.2$ mag AB (5σ measured in small circular apertures of $0''.25$ diameter). Additionally, we reduced all the WFC3/IR data from the complete CANDELS GOODS-South imaging program (PI:

Faber/Ferguson; Grogin et al. 2011; Koekemoer et al. 2011), reaching a varying depth of $H_{160} = 27.5 - 28.3$ mag AB. All our sources are > 1 mag brighter than these limits, and therefore seen at high significance in these images (see Figures 1, 2, and 3). HST photometry is measured on PSF-matched images in small Kron apertures, and is corrected to total fluxes using the H_{160} band image.

Imaging in the K band was particularly important for our analysis, since this is the band in which we took spectroscopic observations. We used a very deep stack of K imaging data consisting of a combination of all available data over the CDF-S. This includes ESO/VLT ISAAC and HAWK-I data, along with PANIC data from Magellan. The final image has exquisite seeing of only $0''.4$. The total K -band photometry was measured in $1''.5$ diameter apertures and was corrected to total fluxes using the observed profiles of stars in the image. We find a limiting magnitude of 26.2 mag AB for a 5σ detection within a $0''.4$ diameter aperture. The actual aperture photometry was performed using the sinc interpolation procedure from Bickerton & Lupton (2013). To estimate the errors on our fluxes, we placed 1000 random apertures scattered throughout the region of the image our targets occupy.

For reliable mass estimates, we additionally measured rest-frame optical photometry at longer wavelengths in the deep *Spitzer*/IRAC (Fazio et al. 2004) [3.6] and [4.5] imaging data over GOODS-South (Dickinson et al. 2003). Due to the large IRAC point-spread function (PSF), we used a sophisticated neighbor subtraction scheme based on a convolution of the J_{125} images to the IRAC PSF. We then perform aperture photometry on the cleaned images in $2''$ diameter apertures, and correct to total fluxes using the growth curves of nearby stars in the field (for more information on the IRAC photometry see Labbé et al. 2010a,b; Oesch et al. 2013; Labbé et al. 2015).

In Figures 1, 2 and 3, we show the i_{775} , H_{160} and K data for each galaxy in our sample with a detected emission line.

3. SPECTROSCOPIC OBSERVATIONS

We observed on January 4, 2013 for a single half night in good conditions with the MOSFIRE instrument. We targeted a single mask in the K -band while the CDFS was visible from the Keck I telescope, yielding a total exposure of 204 minutes with an AB dither pattern. For the offsets between exposures we used both a $1''.0$ and $1''.2$ dither, in order to minimize the impact of potential bad pixels. The seeing in the final stacked spectrum was $0''.7$.

3.1. Reduction and Extraction

The two-dimensional data reduction was performed using a slightly modified version of the MOSFIRE DRP⁹. This pipeline yields two-dimensional, sky-subtracted data for each slitlet, which are rectified and wavelength calibrated, in units of electrons per second. Because MOSFIRE has such high quality optics, the pixel size is almost constant across the field of view and there is little other distortion, so the final rectification is minor. The reductions for the two dither patterns, $1''.0$ and $1''.2$,

were done separately. The two reductions were then averaged, weighted by the exposure time for each separate stack.

All the 2D frames were searched for emission lines by eye, and their fluxes were measured based on an optimal extraction (Horne 1986) using a Gauss-Hermite model. The line model was derived from the brightest line of a given galaxy (i.e. [O III] λ 5007) and was then used to extract the flux of the remaining lines. This was particularly important for lines that were either very faint or sat partially on a night sky line.

In the two right-hand columns of Figures 1, 2 and 3, we show the two-dimensional sky-subtracted spectra for each galaxy with a detected emission line. The sky-subtracted spectra are only shown in the wavelength regions of $H\beta$ and the [O III] doublet.

3.2. Flux Calibration

For the overall zero-point of the spectra, we observed GD71 as spectrophotometric standard. This observation was done with GD71 at an airmass of 1.04 for 120 seconds. This allows us to measure the conversion between e^-s^{-1} and $erg\ s^{-1}\ cm^{-2}\ \text{\AA}^{-1}$, for that exposure.

The above procedure does not deal with the variable seeing and airmass for the observations of our mask. We correct this with a simple average flux correction based on a single star within our mask. The magnitude of the star as computed from the flux calibrated spectrum is $K = 18.24$ mag AB, while its total ($5''$ aperture) magnitude is $K = 18.09$ mag AB. This difference of 0.15 mag represents our estimated amount of flux lost between the typical observation of the CDFS in a $0''.7$ slit and the ideal observation of a star at almost zenith. Therefore, we multiply all of our count rate fluxes by 1.25.

As we have only one flux calibration measurement, we do not have a good estimate of the uncertainties on our calibration. Schenker et al. (2013) found an uncertainty of 15% using a similar approach as we use. Unlike that work, we will not include that uncertainty in our measurements errors.

We tabulate our results in Table 1. This table includes the positions of the objects, the line fluxes without the aperture correction, and the redshift of the object based on the flux weighted centroids of the emission lines. The errors for the fluxes will be discussed in the next section.

3.3. Error Estimates

We estimated the errors for our spectra by simulations. We perform two sets of simulations, one to estimate the statistical errors and a second to estimate the error on the aperture correction. We simulate the flux measurement procedure (§3.3.1) and use simulations to estimate our aperture correction (§3.3.2). As a final check, we use the MOSFIRE exposure time calculator to estimate the theoretical maximum of our signal to noise (§3.3.3).

The simulations rely on using the K imaging data to make templates of our spectroscopic observations. These templates are smoothed to match the seeing in our spectroscopic data ($0''.7$) as compared to the $0''.4$ seeing of the K imaging. These were used to generate artificial images of the lines. These artificial images were further smoothed in the wavelength direction to match the sizes of the lines in the data.

⁹ <https://code.google.com/p/mosfire/>

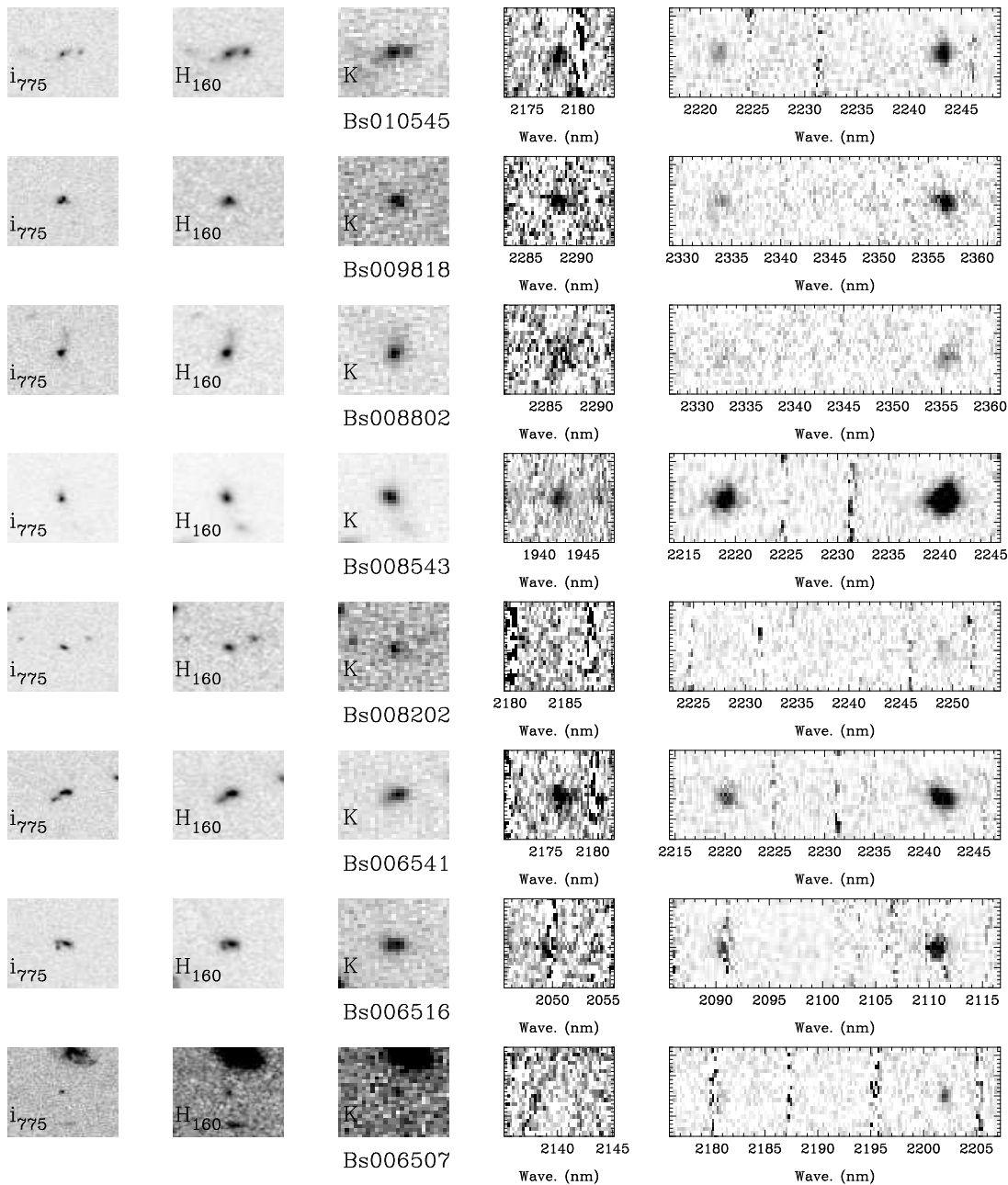


FIG. 1.— Images and MOSFIRE spectra of eight of the $z \sim 3.2 - 3.8$ primary target galaxies. Each image is $4''$ on a side and was rotated such that the slit runs straight up along the y-axis. The spectra cover the two regions where $H\beta$ and the [O III] doublet can be found.

3.3.1. Simulations of the Flux Measurement

Our first set of simulations use the simulated images to compute the error from the model fitting. We place these simulated images in actual data. We placed the simulated emission line at the same wavelength but in other spectra.

The simulated object is normalized to have the same flux as the object was detected with in the spectrum. We then follow the same procedure to estimate the flux, fitting the same order Gauss-Hermite polynomials to model the 5007\AA line, and then use that same model to extract the 4959\AA and $H\beta$ lines.

In general, we find for each object that the modeling process and background variation errors are larger than

accounted for in our statistical errors. How much larger, however, varies depending on how close the emissions are to the night sky background. For example, the target B15573 has statistical errors of 2%, 6% and 7% for 5007\AA , 4959\AA , and $H\beta$, respectively. The simulations show 3%, 6% and 10% for the same lines. The larger error for $H\beta$ comes about from the night sky lines near the emission line, as can be seen in Figure 3. We tabulate these errors as the statistical errors in Table 1.

Kriek et al. (2015) presents measurements of the signal-to-noise as a function of flux measured for MOSDEF, a survey with MOSFIRE of a large sample of galaxies, including a subset at the same redshift range our sample. In general, the signal-to-noise of the sample

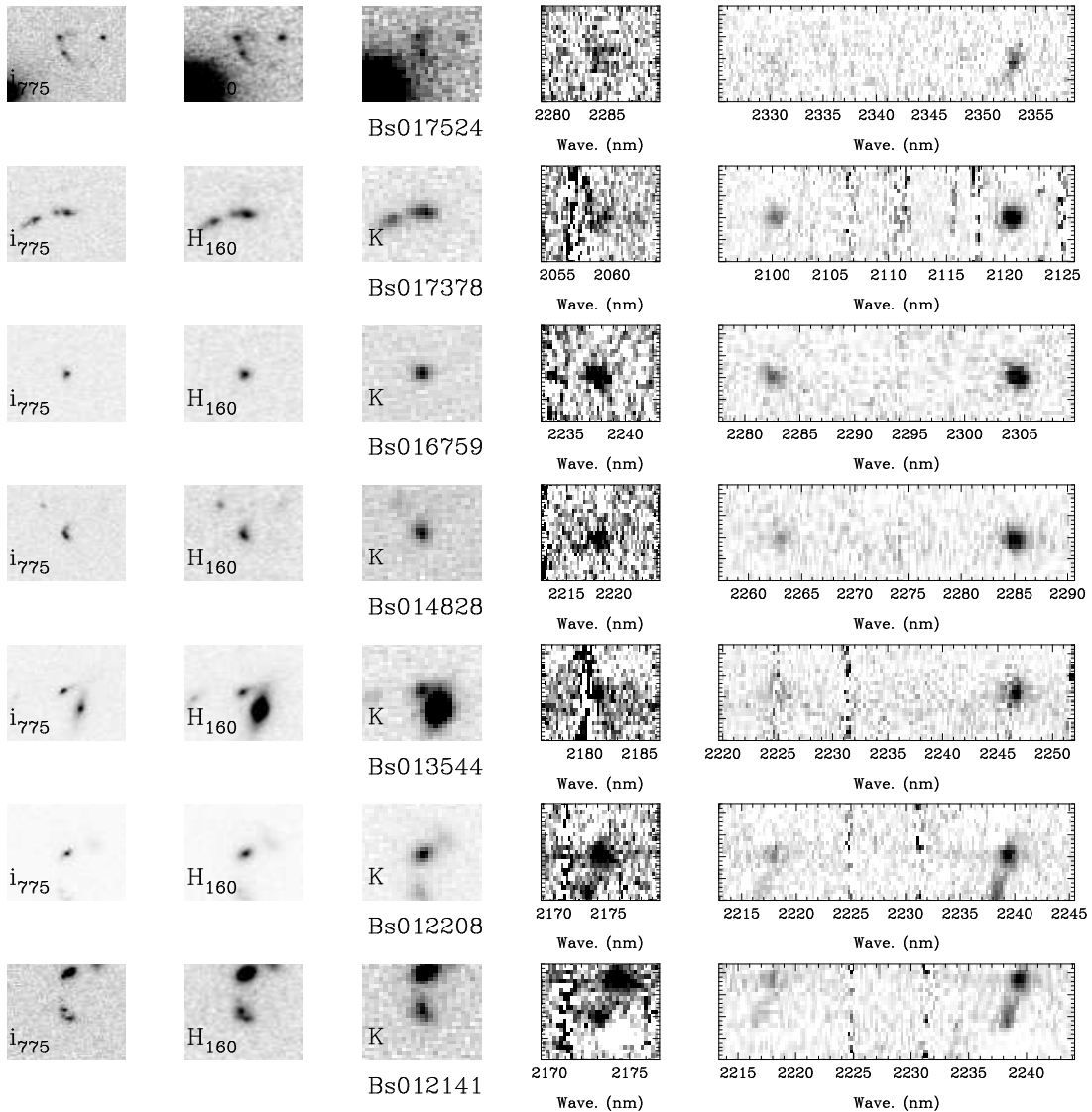


FIG. 2.— As in previous Figure, Images and MOSFIRE spectra of the remaining seven primary targets.

from Kriek et al. (2015) is lower, as expected given the lower typical exposure time for MOSDEF, a 120 minutes compared with our 204 minutes. In general, our results are $\sim 50\%$ in slightly less than twice the exposure time, which is roughly consistent, for the emission lines of interest, with a number of lines in the Kriek et al. (2015) having signal-to-noise values higher than our data with less exposure time. From this we conclude that our data are somewhat better than average, but well within the locus shown in Figure 9 of Kriek et al. (2015).

3.3.2. Simulations of the Aperture Correction

Previous work has found that aperture corrections can be large, even up to a factor of ~ 2 (Erb et al. 2006). We use similar simulations as above to estimate our uncertainties in our aperture corrections. We take the deep K imaging and smooth it to match the seeing in our MOSFIRE spectra. We then place apertures on object at multiple angles. We sum the flux from the object in the aperture and compare that to the total flux. Three objects could not be used for these simulations; B14623,

Bs013544 and Bs017524. In each case the light from the nearby object prevent us from using the object image as a template for the spectrum (see Figures 2 and 3) when measuring the total aperture correction. In §3.2, we find that the slit losses are 0.15 mag. In our simulations, we find the mean value to be 1.25 ± 0.10 , larger than our estimate of 1.15 based on one star. The scatter of 0.10, or 10%, is close to, but smaller than, the estimate of 15% from Stark et al. (2013). We do not include this additional error in Table 1 but have added this to the fluxes in the figures.

These simulations assume that the K band light traces the star-forming regions that generate the emission lines. The actual morphology of the star-forming regions that dominate the line flux cause an additional uncertainty in this aperture correction. Nelson et al. (2015) find, for example, that for $z \sim 1$ galaxies with stellar masses above $10^{9.5} M_{\odot}$ that the length scale of the line emitting region is 10% larger than the stellar continuum, with a slight mass dependence. The difference in the morphologies can lead to an uncertainty in the aperture correction as large

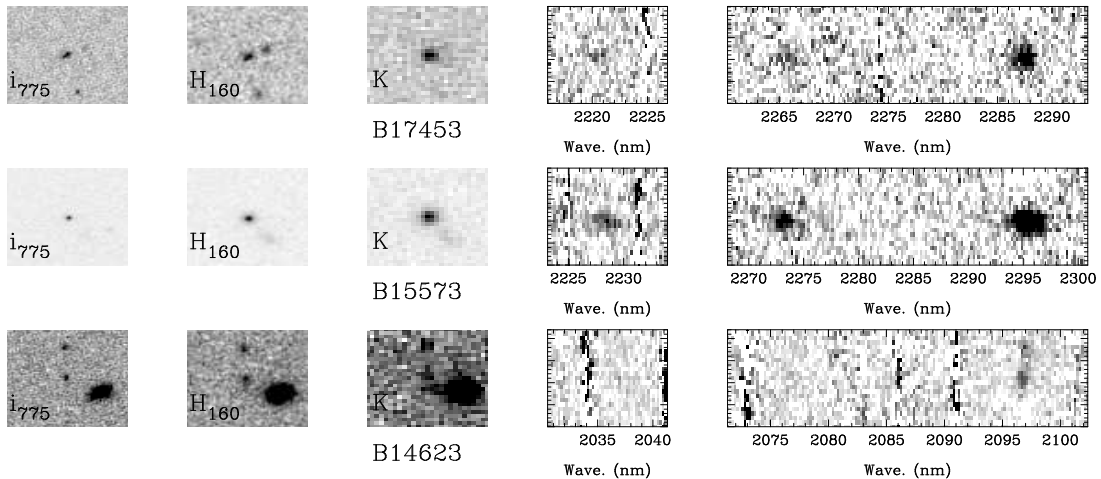


FIG. 3.— As in Figure 1, images and MOSFIRE spectra of the three B_{435} -dropout galaxies, without pre-existing spectra, where we detected emission lines.

as 50% (Erb et al. 2006; Yoshikawa et al. 2010). However, note that these aperture corrections do not affect the main result of this paper, which concerns the ratios of emission lines.

3.3.3. Additional Simulations

MOSFIRE has a sophisticated exposure time calculator. This computes a spectrum specified by the user and places it on top of a real night sky spectrum for Mauna Kea. We perform a set of calculations using this software as a second, independent check on our error estimates. We use the tool to generate artificial spectral lines that matched our selection criteria and typical fluxes. We then place these at random redshifts that match those of the range spanned by our sample. At each redshift, we generated both [O III] lines and $H\beta$. We assume a 200 minute exposure in $0''.7$ FWHM seeing. We did this for two sets of fluxes, using typical flux ratios as found in our sample. The background varies significantly across our redshift range. We mimicked our preselection (see §2.1) before plotting our simulations, which decreases the range of signal-to-noise values possible.

We plot the results in Figure 4. We plot the median values with points and show the range covered by 68% of the simulations with error bars. The points with error bars are from our simulation and represent an upper limit of what should be possible with the MOSFIRE spectrometer, as there are no errors associated with extraction or systematics in the sky subtraction. In general our data have S/N at a given flux below the optimal results. For comparison, we plot the results of Schenker et al. (2013), which are generally at a lower signal-to-noise for the same flux level as our data. Likely, this is because of different conditions during observing. We conclude that our error estimates lie between the theoretical optimum and estimates from other work.

4. ANALYSIS

We detected emission lines for all our primary target galaxies. We also detected lines for three of our fainter LBGs that were secondary targets. We note here we used no pre-selection for these secondary targets. The resulting line fluxes and redshifts are listed in Table 1. For

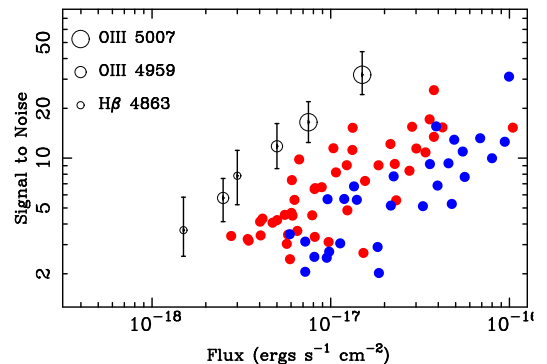


FIG. 4.— The signal to noise as a function of flux for our data (red) and the data from Schenker et al. (2013) (blue). Also plotted (with open circles) are two sets of simulations using the MOSFIRE exposure time calculator for objects with typical fluxes spanning the redshift range of our sample. For these simulations, objects were assigned random redshifts in the range of our sample. At each redshift, we calculated the signal to noise using the exposure time calculator for a fixed flux for all three lines. Because the background varies, the resulting signal to noise changes. We plot the median values and show with error bars the range that encompasses 68% of our simulations. The simulated fluxes are total fluxes, while we plot the observed fluxes from our sample which do not include an aperture correction. Therefore, our data lie below the values from the exposure time calculator. Schenker et al. (2013) find a lower signal to noise at a given flux, likely because of different observing conditions.

almost every spectrum, it was straightforward to identify the [O III] and $H\beta$ lines. For a few targets we do not detect $H\beta$, usually because of night sky emission (see Figures 1, 2, and 3).

For two galaxies, Bs006541 and Bs009818, we additionally detect $H\gamma$ in emission. The part of the night sky that this line falls in, however, is full of Telluric absorption features and our flux calibration is too uncertain in that region, which is why we do not list flux measurements for these lines in Table 1.

The rest-frame optical redshifts tabulated in Table 1 are average values, weighted by the significance of the detected lines. We find excellent agreement between our rest-frame optical redshifts and the pre-existing rest-frame UV redshifts. The average redshift difference is $\delta z = -0.0023 \pm 0.0009$. For the 8 $Ly\alpha$ emitters (LAEs)

among our sample, this corresponds to a velocity offset between Ly α and the [O III] line of 153 ± 60 km s $^{-1}$, possibly indicating somewhat lower outflow velocities than in LAEs at $z \sim 2$ (see also Schenker et al. 2013).

4.1. Estimating the Equivalent Widths

To measure the equivalent widths, we need an estimate of the continuum in the K -band for all our target galaxies. As none of our target galaxies have reliably detected continua, we used the ground based K image to estimate their continuum fluxes. The calibration for flux loss we estimated in §3.2 is, in effect, a total flux in the spatial direction but an aperture of $0''.7$ in the dispersion direction because the data and calibrations are all measured in a slit. We elected to measure the continua expected in the K -band by measuring the magnitude of each target galaxy and the star in a circular aperture with a diameter of $0''.7$. This aperture magnitude for the star is $K = 18.47$ mag AB. Thus, the difference between the flux in the slit and the flux in the aperture is 0.23 mag. We add this offset to each of our K measurements when estimating the continuum to calculate the equivalent width.

Given the strengths of the rest-frame optical emission lines in the K -band, it is clear that these lines will contribute a significant fraction to the total K -band flux. In order to correct for this and to estimate the clean K -band continuum fluxes, we use a line-free star bursting galaxy template from Kinney et al. (1996), to which we add emission lines with the individual strengths that we measured (as listed in Table 1). This template was then rescaled to match the observed, aperture-corrected K magnitude, listed in Table 2, for each target galaxy, from which we obtain the normalization of the line-free continuum.

In Figure 5, we plot the rest-frame equivalent width distribution including all lines detected at $> 2\sigma$. As can be seen, the H β equivalent widths lie in the range $EW_0(\text{H}\beta) = 10\text{--}50$ Å, while the [O III] λ 5007 EW_0 s are very strong with a median of $EW_0 = 200$ Å (i.e. ~ 900 Å observed-frame).

Our observations therefore confirm that high equivalent width rest-frame optical lines result in a very large contribution of emission lines to the rest-frame optical photometry of $z > 4$ galaxies, given the width of the IRAC bands of ~ 1 μm . Ignoring this effect can significantly bias the estimates of stellar masses in such galaxies, and it is therefore very important to derive reliable estimates of the equivalent width distribution of these rest-frame optical lines for large samples of galaxies in the future (see e.g. Schenker et al. 2013).

The errors in the equivalent widths are computed by first adding in quadrature the errors in the aperture-corrected line flux and the error in the K continuum magnitude. We then add the systematic error on the line flux from the aperture correction, 10%, to the term. We tabulate the equivalent width values along with the aperture-corrected fluxes in Table 3

4.2. Properties from Broad Band Photometry: SFRs, Extinction, and Stellar Masses

Using the rest-frame ultra-violet data, we can estimate the UV continuum spectral slope, β , which provides a measurement of the extinction in star-forming galaxies

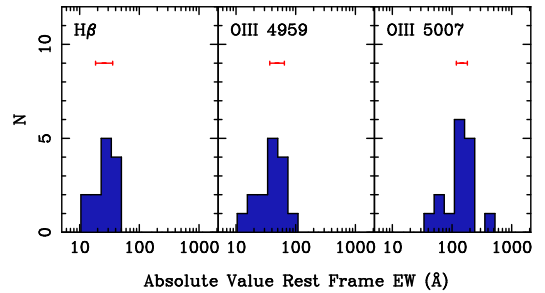


FIG. 5.— Distribution of the absolute value of the rest-frame equivalent widths for detected emission lines in our sample. Each panel separately shows the distribution of equivalent widths based on lines detected at $> 2\sigma$, for H β (left), [O III] λ 4959 (middle), and [O III] λ 5007 (right). We show with red error bars the median error and median equivalent width for each measurement. The error includes both a systematic term of 10% and the error on the flux. The latter is generally a larger fraction of the EW for fainter objects, so the errors increase to smaller EWs. The systematic uncertainty of 10% could be a lower bound, as other work has found values as large as 50%, see Sec. 3.3.2

via the IRX- β relation (see Meurer et al. 1999). The UV slope β is measured from a power-law fit to the broadband filters which sample the rest-frame 1400Å to 2800Å . This includes 4-5 filters from V_{606} to J_{125} , depending on the exact redshift of the sources. In Table 2, we list the measured UV spectral slope. With the dust correction, we can then estimate a star-formation rate from our UV imaging alone (using the relations of Kennicutt 1998). We will call this dust-corrected SFR from the UV, SFR_{UV} .

In order to estimate stellar masses for our galaxies, we use the ZEBRA+ spectral energy distribution fitting code (Oesch et al. 2010) with Bruzual & Charlot (2003) models at sub-solar metallicity ($0.2Z_{\odot}$) and constant star-formation. We verified that the stellar masses do not change significantly if using different assumptions for the star-formation histories, such as exponentially increasing or decreasing functional forms. By fitting models we can estimate star-formation rates and the UV spectral slope (β_{SED}) which are internally consistent with the stellar mass values. We find that the values of β_{SED} are systematically offset by 0.2 from the β we find from fitting a power law to the broad band photometry, in line with differences seen in Finkelstein et al. (2012). For the rest of the paper, we will use the value of β_{SED} unless we specifically state otherwise, as the β_{SED} estimate uses all of the photometry, instead of a subset of four passbands.

Given the large contribution of rest-frame optical emission lines to the K -band photometry, we self-consistently add both nebular emission lines as well as nebular continuum emission to the templates. This is done by converting 80% of ionizing photons from these templates to recombination lines for H and He using case B recombination (Osterbrock & Ferland 2006) and adding metal lines relative to the H β fluxes using the tabulated relations of Anders & Fritze-v. Alvensleben (2003).

5. RESULTS AND DISCUSSION

5.1. Different Indicators of the Star-Formation Rate

We plot the luminosity in H β and the UV star-formation rate in Figure 6, along with simple relation be-

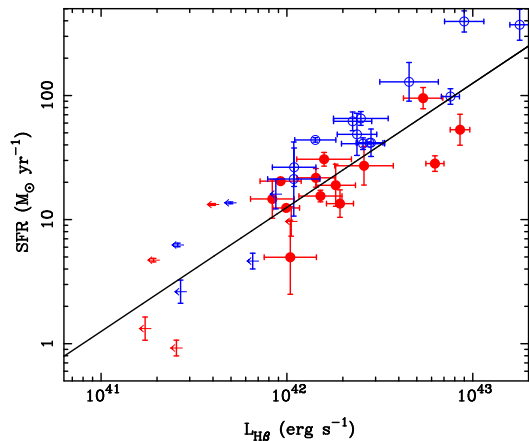


FIG. 6.— Distribution of the the $H\beta$ luminosity compared with our estimates of the dust-corrected UV star-formation rate (red) and star-formation rate derived from fitting spectral energy distributions (blue.) The luminosities are shown only for lines detected at $> 2\sigma$. For comparison we plot the relation between the $H\beta$ luminosity and the star-formation rate from Kennicutt (1998), after correcting the $H\beta$ luminosity from the $H\alpha$ luminosity assuming case B recombination. Both the star-formation rate and the $H\beta$ luminosity have been corrected for dust assuming the extinction relation from Calzetti et al. (2000) with an $R_V = 4.03$ for the UV star-formation rates (red.) The $H\beta$ luminosities were corrected using the extinction from the best-fitting spectral energy distribution (blue) though also assuming the extinction relation from Calzetti et al. (2000). The observed $H\beta$ luminosities are in good agreement with the expectation from the dust corrected UV-based SFR, while the SED based SFR and extinction correction show an offset of 60%. The uncertainty in the dust correction required could easily shift our $H\beta$ luminosities to higher values. This would bring our values inline with our SED based star-formation rates. The large degree of uncertainty in the dust correction, assumptions about metallicities and the star-formation histories mean that either measurement could be in good agreement with the star-formation rates from $H\beta$ luminosities.

tween $H\beta$ and star-formation rate from Kennicutt (1998). This relation assumes case B recombination to estimate the flux ratio of $H\beta$ to $H\alpha$, a factor of 2.86, and converts the initial mass functions to a Chabrier, another factor of 1.8 from the Salpeter assumed by Kennicutt (1998). Both the $H\beta$ luminosity and the UV derived star-formation rate have been corrected for dust extinction assuming the dust extinction from Calzetti et al. (2000) with an $R_V = 4.03$. The extinction was derived from A_{1600} (see §4.2) assuming the Calzetti extinction law, with the stellar continuum having only 0.44 of the extinction of the emission lines. The ratio of the stellar continuum extinction to emission line extinction is highly uncertain in high redshift galaxies, ranging from 0.4 to 1.0 (e.g., Kashino et al. 2013; Salmon et al. 2015). This, in turn, causes a factor of ~ 2 uncertainty in our derived $H\beta$ luminosities (e.g., Yoshikawa et al. 2010). In fact, de Barros et al. (2015) finds the extinction ratio has a star-formation rate dependence and that a value of 0.44 is on the extreme end.

Our galaxies all have been fit with spectral energy distributions, and from those fits we can derive both a value of β and a star-formation rate. In marked contrast to the $H\beta$ and UV star-formation rates, we find that the star-formation rates derived from fitting spectral energy distributions from population synthesis models are higher. Those models should be more self-consistent in handling the extinction and dust from the galaxies.

Even using the extinction correction from the fits of the stellar populations, as we did in Figure 6, our model based star-formation rates are larger than the values derived from the $H\beta$ luminosities. This disagreement was pointed out in Castellano et al. (2014). The SED based star-formation rates are somewhat elevated on average, which is likely a result of different assumptions about metallicities, resulting in different UV spectral slopes for a given age stellar population. In addition, we assume a fixed relation between the extinction of the stellar populations and that of the H_2 regions, but this could be star-formation dependent, metallicity dependent, incorrect, or all three. For our results below, the most important measurements are the stellar mass and the specific star-formation rate. As such, we use the SED based estimates of the star-formation rate as fitting one model to all of the photometry provides a self-consistent estimate of the mass, star-formation rate and stellar extinction.

5.2. The $[O III]/H\beta$ Emission Line Ratios

The primary goal of our observations was to analyze the emission line properties of $z \sim 3.5$ star-forming galaxies. In particular, there is now growing evidence of increasingly high $[O III]/H\beta$ line ratios (e.g. Kewley et al. 2013b) with redshift up to $z \sim 3$, suggesting that the conditions for star-formation might be quite different at high redshift compared to local galaxies. With our sample of 18 galaxies with emission line detections we can now further test these observations at $z \sim 3.5$.

In Figure 7 we plot the $[O III]/H\beta$ ratio as a function of mass. As can be seen, all our galaxies show line ratios larger than 2, with a median of $5.1^{+0.5}_{-0.5}$, which appears to be independent of stellar mass.

For a reference sample of typical local galaxies, we use the MPA-JHU catalog of Brinchmann et al. (2004). This is not a directly comparable sample, as the selection is very different, but provides a large number of galaxies with stellar masses and emission line strengths. We compare with a subset of the DR7 version of the Brinchmann et al. (2004) catalog. We restrict the redshift range to $0.015 < z < 0.08$. The resulting catalog contains 260,647 galaxies covering a wide range of properties and star-formation rates. Each galaxy has a measurement of the $H\beta$ and $[O III]$ flux and equivalent width. In addition, each galaxy has an estimated stellar mass and star-formation rate. The stellar masses come from the imaging data alone, and are thus comparable to our mass estimates.

The Brinchmann et al. (2004) catalog also contains a classification for each source, as either AGN driven or star-formation driven. We use this classification to plot contours of AGN dominated sources and star-formation dominated sources in Figure 7. For our purposes, we combine both AGN and star-forming classifications into one each. We plot those galaxies classified as ‘composite’ in Figure 7, but they are ignored when generating the contours showing where AGN or star-forming galaxies are distributed in the figure.

It is immediately clear from Figure 7 that the LBGs we have observed lie far off of the relationship of star-forming galaxies in the local universe. Many of the galaxies lie in the part of the diagram where sources are classified as AGN in the local universe (illustrated by black contours). The highest mass galaxies lie in a region dom-

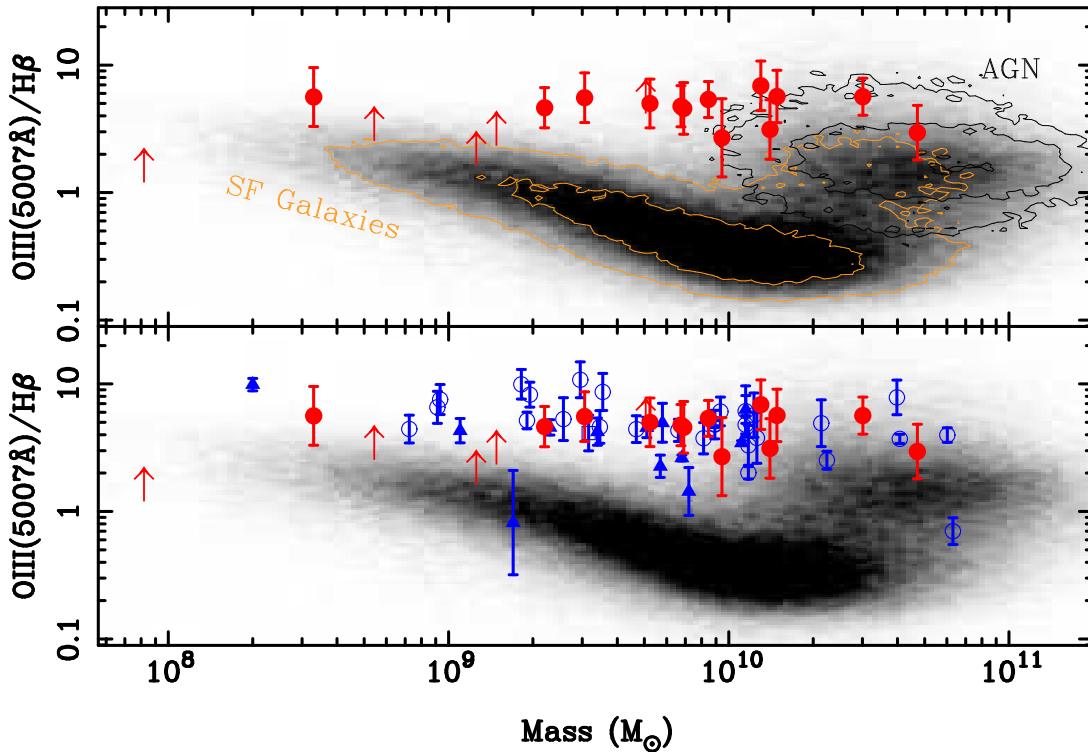


FIG. 7.— The ratio of the [O III] λ 5007 line to $H\beta$ plotted as a function of stellar mass. Our data are shown in red, with upper limits denoted by arrows. In the lower panel, we also overplot the samples of Troncoso et al. (2013) (blue open circles), and the sample of Schenker et al. (2013) (blue solid triangles). We remove all detections of less than 2σ from Schenker et al. (2013). Evidently, all galaxies in our sample and from the literature show high ratios of [O III] to $H\beta$, even at low stellar masses. For comparison, we show underlying grey scale from a sample of galaxies from the SDSS DR7 with line strengths as measured by Brinchmann et al. (2004). The stellar mass estimates are from the broad band photometry alone, mimicking the estimates of the higher redshift galaxies. In the upper panel, we overplot contours of the spectroscopic classifications from Brinchmann et al. (2004), where the black contours show galaxies classified as AGN and the orange contours show galaxies classified as star-forming, based on the ratios of emission line strengths. Clearly, all high-redshift galaxies show line ratios significantly above the local star-forming galaxy population. Furthermore, the line ratios are essentially independent of stellar mass.

inated by AGN, while at lower masses our sources lie in a region which is completely devoid of local galaxies.

In order to increase the sample size of high-redshift sources, we additionally collect data from the literature. First, the work by Maiolino et al. (2008) and Mannucci et al. (2010) provides measurements of [O III] and $H\beta$ line fluxes for a number of LBGs at similar redshifts as our targets. We use the summary of data from Troncoso et al. (2013) which includes stellar masses and star-formation rates as well as line strengths. In fact, the galaxies CDFS-4414 and CDFS-4417 from Maiolino et al. (2008) and Troncoso et al. (2013) are also present in our sample as Bs012141 and Bs012208, respectively.

The sample of Schenker et al. (2013) represents an excellent combination with our data. These authors observed 20 galaxies with MOSFIRE that were selected essentially in the exact same manner as our primary galaxy sample. Namely, they are LBGs, mostly with pre-existing redshift measurements from rest-frame UV spectra. Instead of the GOODS-S field, Schenker et al. (2013) targeted GOODS-N, however. For each of their galaxies Schenker et al. (2013) tabulate $H\beta$ and [O III] flux measurements, along with equivalent widths estimated from the K band continuum. As they tabulate the sum of the two [O III] lines, we multiply their tabulated line flux by 0.75 to estimate the strength of the 5007Å line alone. Schenker et al. (2013) include a 15%

calibration error for their flux estimates. When we estimate the errors on the ratios of the line fluxes, we remove that calibration error.

All high-redshift measurements from the literature are shown as blue symbols in the lower panel of Figure 7, clearly showing that a high ratio of [O III] over $H\beta$ is an ubiquitous feature among star-forming galaxies at $z \sim 3$. We find a mean ratio of $4.8^{+0.8}_{-1.7}$ when we combine our sample with the rest from the literature, after removing the two galaxies in common between our sample and the sample of Maiolino et al. (2008). It is also clear from the Figure, that even after the combination with the larger sample from the literature, we find very little dependence of the line ratio on the stellar mass.

5.3. Possible Contribution by Active Galactic Nuclei

The high observed line ratios in our $z \sim 3.5$ galaxy sample trigger the question, whether these are all dominated by active galactic nuclei (AGN). In the local universe, we generally observe such high values of the [O III] to $H\beta$ ratio only in AGNs (e.g. Juneau et al. 2011). Trump et al. (2011) and Trump et al. (2013) find evidence for active galactic nuclei powering at least some of the $z \sim 1-2$ population and that the lower redshift mass-excitation relations of Juneau et al. (2011) still discriminate between AGN and star-forming galaxies at $z \sim 2$, after only small modifications to slightly higher line ratios. Thus, the high [O III] to $H\beta$ ratio we observe in

Figure 7 could be, for the higher stellar mass galaxies at least, a result of black hole accretion. If the division remains the same at $z \sim 3.5$ as at $z \sim 1.5$, almost all of the galaxies in Figure 7 would be classified as possible AGN.

Given the extremely deep X-ray data over the GOODS-South field, we can test for such AGN contamination in our sample. Using the Chandra 4 Ms catalog of Xue et al. (2011), we search to see if any of our sources are obvious X-ray emitters. Unsurprisingly, none of the X-ray sources are within a point spread function half-width half-maximum of our spectroscopic targets.

We then stack the images of Xue et al. (2011), to see if we detected an average signal from the galaxies in our spectroscopic sample. When performing this stacking, we removed any sources detected in the Xue et al. (2011) catalog. We did this by excising a 7 pixel by 7 pixel box centered on the source, where each pixel is $0''.492$ in size. To build up a background sample, we also extract postage stamps of random parts of the X-ray images. We required that our stamps have no sources within 25 pixels of the stamp center. Thus, both our source stacks and our background stacks will have similar levels of contamination from undetected objects. As the Chandra point spread function becomes larger with increasing radius from the pointing center, we only included background regions with centers whose radii were the same range as our sources.

For both the source and the background stack, we extract a 5 by 5 pixel region at the center from the 0.5 - 2.0 keV soft band image. In our 200 background images, we found 955 counts for an average of 4.8 counts per image. We found 122 counts in our stack of 18 source images for an average 6.8 counts per source. This yields a net of 2.0 counts. This is not, however, statistically significant. We would expect, at random, a stack of 18 images to show 210 counts 17% of the time.

Because AGN luminosity is correlated with the stellar mass of the galaxy, we additionally assembled a stack of the nine highest stellar mass galaxies in our sample. This stack has an average of 8.7 counts per image, for a net 3.9, which only happens 6% of the time. This is still not statistically significant.

We note also that larger samples of galaxies in this redshift range, selected by both photometric and by spectroscopic redshifts, show statistically significant emission, but at luminosities consistent with star-formation (e.g. Cowie et al. 2012). This implies that for typical galaxies in this redshift range, the dominant source of the X-ray emission is not an AGN, but rather star-formation.

Furthermore, for the galaxies for which we do have pre-existing rest-frame UV spectra, we confirmed that none of these sources show any evidence for the presence of an AGN (e.g. based on [N V], [C IV], or broad Ly α emission).

Juneau et al. (2014) argues that, because of the higher flux limits we have in our LBG sample as compared with those from the SDSS, we are biased in our selection such that we will be more likely to find only high [O III] to H β ratio galaxies and likely all of them are AGN. We miss lower [O III] to H β ratio AGN because of selection effects, and also likely miss the other indications of the AGN powering the large ratio of the emission lines. Coil et al. (2015) argue that, in the MOSDEF sample, the selection

effects from Juneau et al. (2014) are not as important as indicated. Rather, the shift to [O III] to H β observed in star forming galaxies comes about because of evolution in those systems.

In summary, we do detect an excess of X-ray events, especially in the higher mass galaxy stack, but it is not statistically significant. Additionally, we do not find any evidence for AGN contamination based on the rest-frame UV spectra. However, we cannot completely rule out the idea that active galactic nuclei generate the high observed emission line ratios at least for some of the galaxies in our sample, in particular if they are optically thick for X-rays.

5.4. *The Conditions of Star-formation in LBGs at $z \sim 3.5$.*

Star-formation can produce high [O III] to H β ratios as seen in our sample. For example, the models of Dopita et al. (2000) and Kewley et al. (2001) have star-forming regions in intense starbursts producing [O III] to H β ratios of ~ 5 . These models do not require especially low metallicity or high electron densities, but they do require high ionization parameters. For example, the peak [O III] to H β in the continuous star-formation model of Kewley et al. (2001) is 5.4 for a model with a metal abundance of $Z = 0.2Z_{\odot}$ and an electron density of 350 cm^{-3} , while the electron density of 10 cm^{-3} model produces a ratio of 5.2. Both models, however, require ionization parameters of $3 \times 10^8 \text{ cm s}^{-1}$, one to two orders of magnitude higher than found in local star-forming galaxies. In fact, low metallicity alone cannot explain the observed ratios, only higher ionization parameters can. When including the impact of radiation pressure in dense star-forming regions, the recent models of Yeh et al. (2013) and Verdolini et al. (2013) can produce even higher [O III] to H β ratios, beyond even what we observe for integrated galaxy light.

In all these models, a high [O III] to H β ratio implies a significantly lower O II line strength, around 70 to 80% of the H β strength. This is indeed observed in high redshift galaxies (see Nakajima et al. 2013).

There are other physical mechanisms proposed to raise the ionization parameter. Stanway et al. (2014) suggests binary star populations can produce significantly elevated [O III] to H β ratios for stellar populations over ~ 100 Myrs. Steidel et al. (2014) shows that a 50,000K blackbody produces the necessary spectrum, in good agreement with the results of Stanway et al. (2014). Interestingly, Erb et al. (2014) finds that the evidence for a harder ionizing spectrum also occurs in the Ly α emission. Steidel et al. (2014), Masters et al. (2014), Shapley et al. (2015), Jones et al. (2015), Sanders et al. (2016) and Cowie et al. (2015) all find that the $z \sim 2$ redshift population requires a different abundance ratio of N/O. Interestingly Dopita et al. (2016) derives a new calibration of the N and O abundance and finds that this N/O shift is not required. The combination of a harder spectrum (e.g., Steidel et al. 2014), or a higher electron density (e.g., Sanders et al. 2016), along with possibly enhanced abundances can explain the location of high redshift galaxies in these excitation diagrams without any AGN contribution.

The above models provide a physical explanation for the large emission line ratios we observe, namely a com-

bination of a large ionization parameter, harder ionizing spectrum, and possibly radiation pressure. This implies that the conditions of star-formation are very different in these high redshift LBGs as compared with galaxies at the same stellar mass in the local universe.

As was highlighted by Brinchmann et al. (2008a) and Brinchmann et al. (2008b), galaxies with strong ionization parameters often have higher specific star-formation rates than the typical star-forming galaxies in the local universe. In Figure 8, we plot the $[\text{O III}]/\text{H}\beta$ specific star-formation rate of galaxies in our sample, combined with the galaxies from Schenker et al. (2013) and Troncoso et al. (2013). We also show the location of local galaxies with star-formation rates of at least $2 M_{\odot} \text{ yr}^{-1}$ and classified as star-formation dominated by Brinchmann et al. (2004). While the typical $z \sim 0$ star-forming galaxy shows low ratios of $[\text{O III}]\lambda 5007$ to $\text{H}\beta$ (only ~ 0.3) and specific star-formation rates (SSFRs) of $\sim 10^{-10} \text{ yr}^{-1}$, a small tail of the local population extends to significantly higher SSFRs and higher line ratios. Interestingly, this tail nicely connects up with the location of the $z \sim 3 - 4$ sample. This suggests that (1) the ionization and/or the radiation pressure of HII regions is connected with the global SSFR, coupling a local and a galaxy-wide property, and (2) a small sub-sample of local star-forming galaxies exhibits similar conditions of star-formation as the $z \sim 3 - 4$ population. These are the galaxies with similarly high SSFRs. Note, however, that these local galaxies on average have a factor $4-5 \times$ lower masses than our $z \sim 3 - 4$ sample.

5.5. How representative is the current sample?

As we have shown above, all of the observed LBGs have extreme star-forming conditions, very different from typical local galaxies. Since LBGs are the dominant contributors to the total star-formation rate at this high redshift (Bouwens et al. 2009), this suggests that star-formation was very different in the early universe compared to the typical local galaxy. However, this depends on how representative our sample is. The galaxies in our sample, and those in Troncoso et al. (2013) and Schenker et al. (2013), are generally selected by $\text{Ly}\alpha$ emission.

Shapley et al. (2003) found that the median Lyman α rest-frame equivalent width for $z \simeq 3$ galaxies was 0 \AA , implying that half of the sample shows emission. Our sample is in agreement with that fraction (8 out of 15 show $\text{Ly}\alpha$ emission). Combining our sample with that of Schenker et al. (2013), however, we find 24 $\text{Ly}\alpha$ emitters out of 36 galaxies. By random chance, we would not expect to draw 24 emitters out of 36 galaxies from the Shapley et al. (2003) sample. Thus it is likely that our the combined sample is biased towards $\text{Ly}\alpha$ emitting LBGs.

When examining the properties of LBGs, Shapley et al. (2003) also found that those galaxies with Lyman α emission generally had lower star-formation rates and lower amounts of dust extinction as measured by bluer values of the UV continuum slope β . We find an average star-formation rate for our sample of $24 \pm 6 M_{\odot} \text{ yr}^{-1}$, well in-line with the expectations of the Lyman α emitters in Shapley et al. (2003). From this, we conclude that our sample, and the ensemble of our sample with that of Schenker et al. (2013), resemble

a sample of moderate Lyman α emitters in properties.

In summary, we may not extend our results to the whole of the LBG population but, that being said, our sample combined with that of Schenker et al. (2013) seems typical for those galaxies with modest Lyman α emission, characterized by lower star-formation rates and lower dust content than typical LBGs.

6. CONCLUSION

We observed 24 galaxies using the MOSFIRE spectrograph, where 15 were selected by having existing rest-frame UV redshift measurements such that we could observe lines with minimal interference from night-sky emission lines. The remaining nine galaxies were $z \sim 4$ LBGs that fell within the mask. For each galaxy, we measured stellar masses, UV spectral slopes, and star-formation rates using existing broad band imaging. From our spectra, we measured the strength of the optical emission lines $\text{H}\beta$ and the $[\text{O III}]$ lines at 4959 and 5007 \AA .

Our main findings are:

- Every galaxy in our primary sample has a detected emission line. Three out of the **nine** galaxies without a known redshift were also detected, pointing to the possibility of a more general survey of galaxies based on a photometric redshift selection alone.
- The ratio of $[\text{O III}]$ to $\text{H}\beta$ is much higher, $5.1_{-0.5}^{+0.5}$ than in similar mass star-forming galaxies in the local universe. When we combine our results with other $z \sim 3$ samples, the ensemble of 67 galaxies has a median value of $4.8_{-1.7}^{+0.8}$, unlike the values of 0.3 to 1 found in the local universe. This implies that the typical conditions for star-formation at $z \sim 3.5$ for UV bright galaxies are very different than in the local universe. These values require a combination of higher ionization parameters, higher electron density, a harder ionizing flux and a different N/O ratio to explain along with lower gas-phase metallicities for the HII regions.
- The line ratio of $[\text{O III}]$ to $\text{H}\beta$ is strongly correlated with specific star-formation in the local universe. A tail of local galaxies with the highest sSFRs shows elevated line ratios similar to what we find for $z \sim 4$ galaxies, thus linking our high-redshift sources with the physical conditions of $z \sim 0$ galaxies. This correlation of sSFR and line ratio implies that local physics within star-forming regions appears to be correlated with the larger scale rate of star-formation across a broad range in galaxy mass scales.

The authors would like to thank David Koo, Renske Smit, Mark Krumholz, and Max Pettini for useful discussions. The authors wish to recognize and acknowledge the very significant cultural role and reverence that the summit of Mauna Kea has always had within the indigenous Hawaiian community. We are most fortunate to have the opportunity to conduct observations from this mountain. Partial support for this work was provided by NASA through Hubble Fellowship grant HF-51278.01 awarded by the Space Telescope Science Insti-

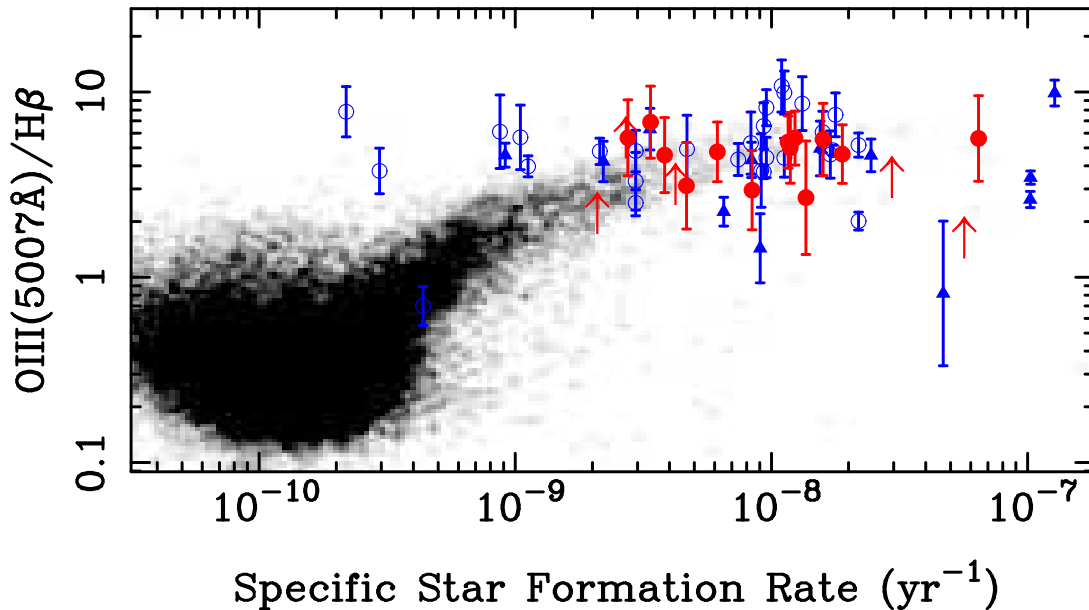


FIG. 8.— The ratio of the [O III] λ 5007 line to $H\beta$ plotted as a function of specific star-formation (the ratio of star-formation to stellar mass). Our data are shown in red, with upper limits denoted by arrows. The blue points represent data from Schenker et al. (2013) (solid triangles) and Troncoso et al. (2013) (open circles), excluding upper limits and the points with specific star-formations beyond the right edge of the plot. For comparison, we plot a sample of galaxies classified as star-forming from the SDSS DR7 with line strengths as measured by Brinchmann et al. (2004) as a grey scale. We remove all galaxies with star-formation rates below $2 M_{\odot} \text{ yr}^{-1}$, the lowest star-formation rate of our high redshift sample. We note that we have purposefully chosen the limits of the grey scale to show the few galaxies in the local universe with the same properties as our high redshift sample. Clearly, all high-redshift galaxies show line ratios significantly above the typical local star-forming galaxy population. However, a small tail of local galaxies extends to higher sSFR, which nicely connects up with the higher [O III] λ 5007 line to $H\beta$ ratios seen in the $z \sim 3 - 4$ population (Brinchmann et al. 2008a,b). Thus, the ionization and/or radiation pressure in local HII region appears to be driven by the overall specific star-formation, therefore coupling a local property with one on a galaxy-wide scale.

tute, which is operated by the Association of Universities for Research in Astronomy, Inc., for NASA, under contract NAS 5-26555. Additionally, this work was partially supported by NASA grant NAG5-7697, and NASA grant HST-GO-11563. This work was further supported in part by the National Science Foundation under Grant PHY-1066293 and the Aspen Center for Physics. This research has made use of the NASA/IPAC Extragalactic

Database (NED) which is operated by the Jet Propulsion Laboratory, California Institute of Technology, under contract with the National Aeronautics and Space Administration.

Facility: *HST* (ACS, WFC3), Keck I (MOSFIRE), VLT (ISAAC, HAWK-I), *Magellan*:Clay (PANIC)

REFERENCES

- Anders, P., & Fritze-v. Alvensleben, U. 2003, *A&A*, 401, 1063
Atek, H., Siana, B., Scarlata, C., et al. 2011, *ApJ*, 743, 121
Balestra, I., Mainieri, V., Popesso, P., et al. 2010, *A&A*, 512, A12
Bickerton, S. J., & Lupton, R. H. 2013, *MNRAS*, 431, 1275
Binette, L., Groves, B., Villar-Martín, M., Fosbury, R. A. E., & Axon, D. J. 2003, *A&A*, 405, 975
Bouwens, R. J., Illingworth, G. D., Franx, M., et al. 2009, *ApJ*, 705, 936
Brinchmann, J., Charlot, S., White, S. D. M., Tremonti, C., Kauffmann, G., Heckman, T., & Brinkmann, J. 2004, *MNRAS*, 351, 1151
Brinchmann, J., Kunth, D., & Durret, F. 2008a, *A&A*, 485, 657
Brinchmann, J., Pettini, M., & Charlot, S. 2008b, *MNRAS*, 385, 769
Bruzual, G., & Charlot, S. 2003, *MNRAS*, 344, 1000
Calzetti, D., Armus, L., Bohlin, R. C., Kinney, A. L., Koornneef, J., & Storchi-Bergmann, T. 2000, *ApJ*, 533, 682
Cardamone, C., Schawinski, K., Sarzi, M., et al. 2009, *MNRAS*, 399, 1191
Castellano, M., Sommariva, V., Fontana, A., et al. 2014, *A&A*, 566, A19
Coil, A. L., Aird, J., Reddy, N., et al. 2015, *ApJ*, 801, 35
Cowie, L. L., Barger, A. J., & Hasinger, G. 2012, *ApJ*, 748, 50
Cowie, L. L., Barger, A. J., & Songaila, A. 2015, arXiv:1512.00017
de Barros, S., Schaerer, D., & Stark, D. P. 2014, *A&A*, 563, A81
de Barros, S., Reddy, N., & Shivaee, I. 2015, arXiv:1509.05055
Dickinson, M., Giavalisco, M., & GOODS Team. 2003, in *The Mass of Galaxies at Low and High Redshift*, ed. R. Bender & A. Renzini, 324
Dopita, M. A., Kewley, L. J., Heisler, C. A., & Sutherland, R. S. 2000, *ApJ*, 542, 224
Dopita, M. A., Kewley, L. J., Sutherland, R. S., & Nicholls, D. C. 2016, arXiv:1601.01337
Erb, D. K., Steidel, C. C., Shapley, A. E., Pettini, M., Reddy, N. A., & Adelberger, K. L. 2006, *ApJ*, 647, 128
Erb, D. K., Steidel, C. C., Trainor, R. F., et al. 2014, *ApJ*, 795, 33
Fazio, G. G., Hora, J. L., Allen, L. E., et al. 2004, *ApJS*, 154, 10
Finkelstein, S. L., Papovich, C., Salmon, B., et al. 2012, *ApJ*, 756, 164
Fosbury, R. A. E., Villar-Martín, M., Humphrey, A., et al. 2003, *ApJ*, 596, 797
Giavalisco, M., Ferguson, H. C., Koekemoer, A. M., et al. 2004, *ApJ*, 600, L93
González, V., Bouwens, R. J., Labbé, I., Illingworth, G., Oesch, P., Franx, M., & Magee, D. 2012, *ApJ*, 755, 148
Grogin, N. A., Kocevski, D. D., Faber, S. M., et al. 2011, *ApJS*, 197, 35
Horne, K. 1986, *PASP*, 98, 609
Jones, T., Martin, C., & Cooper, M. C. 2015, *ApJ*, 813, 126
Juneau, S., Dickinson, M., Alexander, D. M., & Salim, S. 2011, *ApJ*, 736, 104
Juneau, S., Bournaud, F., Charlot, S., et al. 2014, *ApJ*, 788, 88

TABLE 1
MEASUREMENTS FROM THE SPECTRA.

Id	α (J2000)	δ (J2000)	$f_{H\beta}$ (10^{-18} erg s $^{-1}$ cm $^{-2}$)	f_{4959} (10^{-18} erg s $^{-1}$ cm $^{-2}$)	f_{5007} (10^{-18} erg s $^{-1}$ cm $^{-2}$)	z
Bs006507	3:32:14.78	-27:52:37.70	0.1 \pm 1.8	2.4 \pm 4.0	5.8 \pm 1.7	3.39810 \pm 0.04528
Bs006516	3:32:14.79	-27:50:46.50	3.9 \pm 2.4	9.7 \pm 3.1	27.6 \pm 3.3	3.21583 \pm 0.04928
Bs006541	3:32:14.82	-27:52:04.61	8.9 \pm 1.3	13.2 \pm 1.2	42.2 \pm 2.8	3.47730 \pm 0.02188
Bs008202	3:32:17.43	-27:52:01.22	0.8 \pm 0.9	1.3 \pm 0.9	5.9 \pm 2.4	3.49227 \pm 0.09104
Bs008543	3:32:17.89	-27:50:50.14	18.5 \pm 2.0	37.8 \pm 2.8	104.5 \pm 6.8	3.47484 \pm 0.01968
Bs008802	3:32:18.28	-27:51:58.91	5.7 \pm 1.9	6.5 \pm 1.8	15.2 \pm 5.7	3.70487 \pm 0.03714
Bs009818	3:32:19.81	-27:53:00.86	6.1 \pm 1.4	10.3 \pm 0.9	33.9 \pm 3.1	3.70715 \pm 0.03825
Bs010545	3:32:20.97	-27:50:22.35	4.0 \pm 1.0	6.1 \pm 0.8	22.8 \pm 2.5	3.48041 \pm 0.03325
Bs012141	3:32:23.24	-27:51:57.87	3.4 \pm 1.1	3.5 \pm 1.1	10.7 \pm 1.3	3.47083 \pm 0.05601
Bs012208	3:32:23.34	-27:51:56.87	7.9 \pm 1.7	8.1 \pm 2.4	23.2 \pm 4.2	3.47271 \pm 0.03522
Bs013544	3:32:25.15	-27:48:52.62	4.2 \pm 1.0	8.1 \pm 1.2	28.5 \pm 1.8	3.48718 \pm 0.03807
Bs014828	3:32:26.76	-27:52:25.91	6.0 \pm 1.3	5.5 \pm 1.2	30.1 \pm 2.6	3.56387 \pm 0.02811
Bs016759	3:32:29.14	-27:48:52.62	8.2 \pm 1.2	13.3 \pm 0.9	37.8 \pm 1.5	3.60331 \pm 0.03017
Bs017378	3:32:29.93	-27:49:28.28	4.7 \pm 1.2	6.3 \pm 1.1	21.6 \pm 1.8	3.23547 \pm 0.02700
Bs017524	3:32:30.10	-27:50:57.73	2.5 \pm 1.8	4.1 \pm 1.2	12.4 \pm 2.6	3.69918 \pm 0.06252
B14623	3:32:26.50	-27:51:02.21	0.2 \pm 0.4	0.5 \pm 0.9	2.0 \pm 1.7	3.18798 \pm 0.06445
B15573	3:32:27.64	-27:50:59.68	6.7 \pm 0.7	12.3 \pm 1.4	35.8 \pm 2.1	3.58419 \pm 0.02541
B17453	3:32:30.02	-27:50:41.35	2.8 \pm 0.8	5.0 \pm 1.2	15.6 \pm 2.1	3.56878 \pm 0.04179

- Kakazu, Y., Cowie, L. L., & Hu, E. M. 2007, *ApJ*, 668, 853
Kashino, D., Silverman, J. D., Rodighiero, G., et al. 2013, *ApJ*, 777, L8
Kennicutt, Jr., R. C. 1998, *ARA&A*, 36, 189
Kewley, L. J., Dopita, M. A., Leitherer, C., et al. 2013, *ApJ*, 774, 100
Kewley, L. J., Dopita, M. A., Sutherland, R. S., Heisler, C. A., & Trevena, J. 2001, *ApJ*, 556, 121
Kewley, L. J., Maier, C., Yabe, K., Ohta, K., Akiyama, M., Dopita, M. A., & Yuan, T. 2013b, *ApJ*, 774, L10
Kinney, A. L., Calzetti, D., Bohlin, R. C., McQuade, K., Storchi-Bergmann, T., & Schmitt, H. R. 1996, *ApJ*, 467, 38
Koekemoer, A. M., Faber, S. M., Ferguson, H. C., et al. 2011, *ApJS*, 197, 36
Kriek, M., Shapley, A. E., Reddy, N. A., et al. 2015, *ApJS*, 218, 15
Labbé, I., Gonzalez, V., Bouwens, R. J., et al. 2010a, *ApJ*, 716, L103
Labbé, I., Gonzalez, V., Bouwens, R. J., et al. 2010b, *ApJ*, 708, L26
Labbé, I., Oesch, P. A., Bouwens, R. J., et al. 2013, *ApJ*, 777, L19
Labbé, I., Oesch, P. A., Illingworth, G. D., et al. 2015, *ApJS*, 221, 23
Lee, K.-S., Alberts, S., Atlee, D., et al. 2012, *ApJ*, 758, L31
Maiolino, R., Nagao, T., Grazian, A., et al. 2008, *A&A*, 488, 463
Mannucci, F., Cresci, G., Maiolino, R., Marconi, A., & Gnerucci, A. 2010, *MNRAS*, 408, 2115
Mannucci, F., Cresci, G., Maiolino, R., et al. 2009, *MNRAS*, 398, 1915
Maseda, M. V., van der Wel, A., da Cunha, E., et al. 2013, *ApJ*, 778, L22
Masters, D., McCarthy, P., Siana, B., et al. 2014, *ApJ*, 785, 153
McLean, I. S., et al. 2012, in *Society of Photo-Optical Instrumentation Engineers (SPIE) Conference Series*, Vol. 8446, Society of Photo-Optical Instrumentation Engineers (SPIE) Conference Series
Meurer, G. R., Heckman, T. M., & Calzetti, D. 1999, *ApJ*, 521, 64
Nakajima, K., Ouchi, M., Shimasaku, K., Hashimoto, T., Ono, Y., & Lee, J. C. 2013, *ApJ*, 769, 3
Nelson, E. J., van Dokkum, P. G., Förster Schreiber, N. M., et al. 2015, *arXiv:1507.03999*
Oesch, P. A., Carollo, C. M., Feldmann, R., et al. 2010, *ApJ*, 714, L47
Oesch, P. A., Labbé, I., Bouwens, R. J., et al. 2013, *ApJ*, 772, 136
Osterbrock, D. E., & Ferland, G. J. 2006, *Astrophysics of gaseous nebulae and active galactic nuclei*
Rich, J. A., Kewley, L. J., & Dopita, M. A. 2014, *ApJ*, 781, L12
Salmon, B., Papovich, C., Long, J., et al. 2015, *arXiv:1512.05396*
Sanders, R. L., Shapley, A. E., Kriek, M., et al. 2016, *ApJ*, 816, 23
Schaerer, D., & de Barros, S. 2009, *A&A*, 502, 423
Schenker, M. A., Ellis, R. S., Konidaris, N. P., & Stark, D. P. 2013, *arXiv:1306.1518*
Shapley, A. E., Reddy, N. A., Kriek, M., et al. 2015, *ApJ*, 801, 88
Shapley, A. E., Steidel, C. C., Pettini, M., & Adelberger, K. L. 2003, *ApJ*, 588, 65
Shim, H., Chary, R.-R., Dickinson, M., Lin, L., Spinrad, H., Stern, D., & Yan, C.-H. 2011, *ApJ*, 738, 69
Shirazi, M., Brinchmann, J., & Rahmati, A. 2014, *ApJ*, 787, 120
Smit, R., Bouwens, R. J., Labbé, I., et al. 2014, *ApJ*, 784, 58
Stanway, E. R., Eldridge, J. J., Greis, S. M. L., Davies, L. J. M., Wilkins, S. M., & Bremer, M. N. 2014, *MNRAS*, 444, 3466
Stark, D. P., Ellis, R. S., Bunker, A., Bundy, K., Targett, T., Benson, A., & Lacy, M. 2009, *ApJ*, 697, 1493
Stark, D. P., Schenker, M. A., Ellis, R., Robertson, B., McLure, R., & Dunlop, J. 2013, *ApJ*, 763, 129
Steidel, C. C., Giavalisco, M., Pettini, M., Dickinson, M., & Adelberger, K. L. 1996, *ApJ*, 462, L17
Steidel, C. C., Rudie, G. C., Strom, A. L., et al. 2014, *ApJ*, 795, 165
Troncoso, P., Maiolino, R., Sommariva, V., et al. 2014, *A&A*, 563, A58
Trump, J. R., Konidaris, N. P., Barro, G., et al. 2013, *ApJ*, 763, L6
Trump, J. R., Weiner, B. J., Scarlata, C., et al. 2011, *ApJ*, 743, 144
van der Wel, A., Rix, H.-W., Wuyts, S., et al. 2011, *ApJ*, 730, 38
Vanzella, E., Cristiani, S., Dickinson, M., et al. 2008, *A&A*, 478, 83
Verdolini, S., Yeh, S. C. C., Krumholz, M. R., Matzner, C. D., & Tielens, A. G. G. M. 2013, *ApJ*, 769, 12
Xia, L., Malhotra, S., Rhoads, J., et al. 2012, *AJ*, 144, 28
Xue, Y. Q., Luo, B., Brandt, W. N., et al. 2011, *ApJS*, 195, 10
Yeh, S. C. C., Verdolini, S., Krumholz, M. R., Matzner, C. D., & Tielens, A. G. G. M. 2013, *ApJ*, 769, 11
Yoshikawa, T., Akiyama, M., Kajisawa, M., et al. 2010, *ApJ*, 718, 112

TABLE 2
PHOTOMETRY AND PHOTOMETRIC DERIVED MEASUREMENTS

Id	i_{775} (mag AB)	K (mag AB)	Mass ($10^9 M_{\odot}$)	β	β_{SED}	SFR _{UV} ($M_{\odot} \text{ yr}^{-1}$)	sSFR _{UV} (Gyr^{-1})	SFR _{SED} ($M_{\odot} \text{ yr}^{-1}$)	sSFR _{SED} (Gyr^{-1})
Bs006507	26.93 ± 0.13	26.45 ± 0.21	0.08 ± 0.08	-2.55 ± 0.35	-2.06 ± 0.16	0.9 ± 0.1	11.4 ± 1.7	4.6 ± 0.7	57.2 ± 8.3
Bs006516	23.84 ± 0.01	23.94 ± 0.04	3.64 ± 0.30	-2.41 ± 0.21	-2.30 ± 0.02	13.2 ± 0.2	3.6 ± 0.1	13.6 ± 0.2	3.7 ± 0.1
Bs006541	23.95 ± 0.02	23.44 ± 0.02	5.25 ± 0.46	-2.35 ± 0.13	-1.82 ± 0.03	12.4 ± 0.2	2.4 ± 0.0	41.5 ± 0.8	7.9 ± 0.1
Bs008202	25.11 ± 0.03	24.96 ± 0.11	1.11 ± 0.27	-2.40 ± 0.17	-2.24 ± 0.05	4.7 ± 0.2	4.2 ± 0.1	6.3 ± 0.2	5.6 ± 0.2
Bs008543	23.62 ± 0.01	22.73 ± 0.01	23.95 ± 3.17	-1.62 ± 0.19	-1.23 ± 0.07	53.0 ± 15.2	2.2 ± 0.6	371.6 ± 106.7	15.5 ± 4.5
Bs008802	23.96 ± 0.02	23.80 ± 0.04	7.56 ± 1.16	-1.70 ± 0.22	-1.41 ± 0.06	27.2 ± 9.7	3.6 ± 1.3	128.9 ± 46.2	17.0 ± 6.1
Bs009818	24.38 ± 0.02	24.18 ± 0.06	2.65 ± 0.53	-1.92 ± 0.23	-1.78 ± 0.03	18.9 ± 7.4	7.1 ± 2.8	48.6 ± 19.0	18.3 ± 7.2
Bs010545	24.59 ± 0.03	24.01 ± 0.04	9.98 ± 3.46	-1.72 ± 0.11	-1.45 ± 0.07	15.5 ± 1.7	1.6 ± 0.2	40.9 ± 4.4	4.1 ± 0.4
Bs012141	24.19 ± 0.03	24.13 ± 0.04	10.90 ± 1.60	-1.61 ± 0.12	-1.38 ± 0.04	30.7 ± 3.9	2.8 ± 0.4	65.3 ± 8.3	6.0 ± 0.8
Bs012208	23.40 ± 0.01	22.63 ± 0.01	36.58 ± 2.99	-1.41 ± 0.15	-1.14 ± 0.04	95.2 ± 18.7	2.6 ± 0.5	395.4 ± 77.7	10.8 ± 2.1
Bs013544	23.96 ± 0.01	23.47 ± 0.02	9.56 ± 1.31	-2.00 ± 0.10	-1.77 ± 0.04	20.4 ± 0.8	2.1 ± 0.1	43.9 ± 1.8	4.6 ± 0.2
Bs014828	23.95 ± 0.02	23.58 ± 0.03	4.42 ± 0.74	-1.99 ± 0.14	-1.76 ± 0.04	21.7 ± 3.7	4.9 ± 0.8	62.0 ± 10.7	14.0 ± 2.4
Bs016759	24.54 ± 0.02	23.85 ± 0.04	1.94 ± 0.20	-2.01 ± 0.17	-1.81 ± 0.03	13.5 ± 3.4	6.9 ± 1.8	41.6 ± 10.6	21.5 ± 5.5
Bs017378	24.05 ± 0.02	23.87 ± 0.03	5.13 ± 0.56	-2.03 ± 0.23	-1.88 ± 0.05	14.7 ± 5.2	2.9 ± 1.0	26.4 ± 9.4	5.1 ± 1.8
Bs017524	25.15 ± 0.05	25.00 ± 0.08	0.53 ± 0.09	-1.92 ± 0.18	-2.02 ± 0.09	9.7 ± 2.6	18.3 ± 5.0	16.0 ± 4.4	30.4 ± 8.3
B14623	26.81 ± 0.15	26.49 ± 0.38	0.88 ± 0.53	-1.96 ± 0.14	-1.73 ± 0.13	1.3 ± 0.3	1.5 ± 0.3	2.6 ± 0.6	3.0 ± 0.6
B15573	25.09 ± 0.03	23.60 ± 0.03	6.76 ± 1.09	-1.28 ± 0.13	-1.18 ± 0.02	28.3 ± 4.1	4.2 ± 0.6	98.2 ± 14.1	14.5 ± 2.1
B17453	26.08 ± 0.07	24.75 ± 0.08	0.32 ± 0.03	-1.76 ± 0.38	-1.73 ± 0.04	5.0 ± 3.4	15.4 ± 10.6	21.2 ± 14.6	65.9 ± 45.3

TABLE 3
EQUIVALENT WIDTH MEASUREMENTS

Id	$f_{c,H\beta}$ ($10^{-18} \text{ ergs}^{-1} \text{ cm}^{-2}$)	EW _{Hβ} (\AA)	$f_{c,4959}$ ($10^{-18} \text{ ergs}^{-1} \text{ cm}^{-2}$)	EW ₄₉₅₉ (\AA)	$f_{c,5007}$ ($10^{-18} \text{ ergs}^{-1} \text{ cm}^{-2}$)	EW ₅₀₀₇ (\AA)
Bs006507	0.1 ± 2.2	-27.2 ± 566.7	2.9 ± 5.3	-782.8 ± 1419.3	7.2 ± 2.8	-1920.6 ± 880.2
Bs006516	4.9 ± 3.5	-101.1 ± 73.1	12.2 ± 5.1	-254.0 ± 107.6	34.5 ± 7.6	-721.6 ± 162.9
Bs006541	11.1 ± 2.8	-149.1 ± 37.4	16.5 ± 3.1	-221.9 ± 42.5	52.8 ± 8.7	-710.6 ± 119.6
Bs008202	1.0 ± 1.3	-49.2 ± 59.8	1.6 ± 1.3	-77.9 ± 61.4	7.4 ± 3.8	-354.7 ± 185.4
Bs008543	23.2 ± 4.9	-171.8 ± 36.3	47.2 ± 8.2	-351.6 ± 61.6	131.0 ± 21.6	-973.9 ± 161.8
Bs008802	7.1 ± 3.1	-104.3 ± 45.0	8.1 ± 3.1	-119.6 ± 45.3	19.1 ± 9.0	-281.8 ± 134.2
Bs009818	7.6 ± 2.5	-162.5 ± 53.8	12.9 ± 2.4	-275.8 ± 56.8	42.4 ± 8.2	-905.5 ± 190.2
Bs010545	5.0 ± 1.7	-110.1 ± 38.0	7.6 ± 1.8	-166.3 ± 40.1	28.5 ± 5.9	-629.2 ± 135.6
Bs012141	4.3 ± 1.7	-95.3 ± 39.1	4.3 ± 1.8	-96.5 ± 40.4	13.4 ± 3.0	-299.2 ± 68.3
Bs012208	9.8 ± 3.2	-51.2 ± 16.5	10.2 ± 4.1	-53.0 ± 21.2	29.1 ± 8.1	-153.2 ± 42.9
Bs013544	5.2 ± 1.7	-65.2 ± 21.7	10.1 ± 2.6	-128.5 ± 32.8	35.7 ± 5.9	-454.3 ± 76.1
Bs014828	7.5 ± 2.4	-105.7 ± 33.5	6.9 ± 2.2	-96.9 ± 31.2	37.7 ± 7.1	-532.1 ± 102.4
Bs016759	10.2 ± 2.6	-189.5 ± 48.6	16.6 ± 2.8	-308.0 ± 54.5	47.2 ± 6.5	-879.0 ± 136.9
Bs017378	5.9 ± 2.0	-108.8 ± 37.8	7.8 ± 2.2	-144.7 ± 40.7	27.0 ± 4.9	-500.7 ± 93.9
Bs017524	3.1 ± 2.5	-139.0 ± 115.7	5.1 ± 2.0	-230.5 ± 93.0	15.5 ± 4.8	-706.6 ± 227.4
B14623	0.2 ± 0.6	-46.4 ± 117.4	0.6 ± 1.1	-122.1 ± 235.7	2.5 ± 2.4	-504.0 ± 523.1
B15573	8.3 ± 1.7	-120.5 ± 24.9	15.4 ± 3.2	-223.4 ± 47.8	44.7 ± 7.1	-651.5 ± 107.9
B17453	3.5 ± 1.4	-158.6 ± 64.4	6.3 ± 2.1	-287.4 ± 100.6	19.5 ± 4.6	-894.4 ± 231.6